Center for Turbulence Research
Annual Research Briefs 2010

Full-system RANS of the HyShot II scramjet Part 1: Numerics and non-reactive simulations

By R. Pečnik, V. E. Terrapon, F. Ham AND G. Iaccarino

1. Motivation and objectives

The development of computational tools that can faithfully reproduce high-Mach number flight conditions is fundamental to improving our ability to realize hypersonic vehicles, especially because physical prototyping is challenging and extremely expensive. Of special consideration in the development of hypersonic vehicles is accurate evaluation of the safety and operability margins associated with specific design solutions, given our relatively limited experience with sustained hypersonic flight.

The theoretical performance advantage of scramjets over rockets in hypersonic flight has been well known since the 1950s. For this reason, significant scramjet research has been conducted in many parts of the world. Mainly, three different experimental approaches have been followed to gain experience with and insight into scramjet propulsion systems: ground testing in continuous flow facilities for Mach<7, high enthalpy shock tunnels with flow durations of the order of 1–10 ms for Mach>7 and more *realistic* ballistic reentry vehicle experiments. A typical example for such a reentry vehicle is the Hyshot flight project devised by the University of Queensland (Smart *et al.* 2006). Postflight data analysis confirmed the presence of supersonic combustion during an approximately 3 s test window at altitudes of 35–29 km. However, because of to a radar tracking failure, the exact trajectory is not known. To obtain a more comprehensive data set, a ground-based experiment with a 1:1 model for the presumed same conditions as for the flight experiment was conducted by the German Aerospace Center (DLR) in the high enthalpy shock tunnel (Gardner *et al.* 2004). However, to further complement the data, numerical simulations are necessary to gain insight in the physics of scramjet engines.

With this objective, we developed a computational infrastructure to solve the Reynolds-averaged Navier-Stokes equations and to validate the code with the HEG experimental data and to gain detailed information of the flow through the Hyshot II scramjet engine. This is the first of a two-part study of the HyShot II scramjet. It describes the flow solver that has been developed and then used for the simulation of the non-reactive flow through the scramjet engine for validation. Part 2 will then focus on the reactive cases.

2. Reynolds-averaged Navier-Stokes solver

A parallel solver for the solution of the compressible Navier-Stokes equations on unstructured meshes has been developed based on a finite volume formulation and implicit time-integration on arbitrary polyhedral meshes. The governing equations are written in conservative form as

$$\frac{\partial}{\partial t}\int_{\Omega}\mathbf{U}d\Omega+\int_{\partial\Omega}\left[\mathbf{F}\left(\mathbf{U}\right)-\mathbf{F}_v\left(\mathbf{U}\right)\right]dA=0\ , \tag{2.1}$$

where $\mathbf{U}=\mathbf{U}(\mathbf{x},t)$ is the state variable, $\mathbf{F}(\mathbf{U})$ and $\mathbf{F}_v(\mathbf{U})$ are the convective and viscous fluxes, respectively, and Ω and $\partial\Omega$ are the physical domain of interest and its boundary.

In particular, we consider

$$\begin{aligned} \mathbf{U} &= [\rho,\ \rho\mathbf{v},\ E,\ \rho\phi_i]^T \\ \mathbf{F}(\mathbf{U}) &= [\mathbf{n}\cdot\rho\mathbf{v},\ \mathbf{v}\left(\mathbf{n}\cdot\rho\mathbf{v}\right)+p\mathbf{n},\ \left(E+p\right)\left(\mathbf{v}\cdot\mathbf{n}\right),\ \mathbf{n}\cdot\rho\mathbf{v}\phi_i]^T \\ \mathbf{F}(\mathbf{U})_v &= [0,\ \mathbf{n}\cdot\Pi,\ \mathbf{v}\cdot(\mathbf{n}\cdot\Pi)+\mathbf{n}\cdot\mathbf{Q},\ \mathbf{n}\cdot C_i\ \nabla\phi_i]^T, \end{aligned} \tag{2.2}$$

where ρ, $\mathbf{v}$, p, E, Π, $\mathbf{Q}$, ϕ_i, C_i, $\mathbf{n}$ represent density, Cartesian velocity vector, pressure, total energy, stress tensor, heat flux vector, generic scalar, diffusivity constant and outward pointing unit vector normal to the surface, respectively. The discretization scheme is based on a finite volume formulation and implicit time-integration on arbitrary polyhedral mesh elements. The code is entirely written in C++ and uses subdomain decomposition and the Message Passing Interface (MPI) as the parallel infrastructure.

The flow quantities are stored in the cell centers and the governing equations are integrated in conservative form:

$$\frac{\partial\mathbf{U}}{\partial t} = -\mathbf{R}\left(\mathbf{U}\right), \tag{2.3}$$

with

$$\mathbf{R}\left(\mathbf{U}\right) = \frac{1}{V}\sum_f \left[\mathbf{F}\left(\mathbf{U}\right) - \mathbf{F}_v\left(\mathbf{U}\right)\right] A_f\ . \tag{2.4}$$

2.1. *Convective fluxes*

In the past three decades, many different approaches have been introduced to evaluate convective fluxes; Druguet *et al.* (2005) provide a comprehensive comparison of various methods. In general, for hypersonic applications approximate Riemann solvers are most commonly used. These solvers approximate the wavespeeds (eigenvalues of the Jacobian matrix) from an arithmetic or a square-root average of the left and right states of the Riemann problem (Roe 1981). This procedure leads to an underestimation of the expansion-wave velocity, the so-called expansion shock. Another important limitation of these schemes is the so-called carbuncle phenomenon observed, for example, at the stagnation region of blunt bodies in hypersonic flows. In this region the convective velocity is relatively small compared to the sound speed, and errors are *trapped* and deteriorate the solution accuracy (Candler *et al.* 2007; Quirk 1994).

Different solutions have been proposed in the literature and can be separated into two families: eigenvalue-limiting methods and hybrid approaches, given in van Leer *et al.* (1989); Sanders *et al.* (1998); Nompelis *et al.* (2005), and Nishikawa & Kitamura (2008).

The approximate Riemann solver used in the present context is the HLLC scheme proposed by Toro *et al.* (1994) and Batten *et al.* (1997). In this method the entropy condition is enforced (no entropy violating discontinuous waves, called rarefaction shocks), and the scheme preserves positivity without the need for additional corrections.

The convective flux is evaluated as

$$\mathbf{F}^{HLLC} = \begin{cases} \mathbf{F}\left(\mathbf{U}_l\right) & \text{if } S_L > 0 \\ \mathbf{F}\left(\mathbf{U}_l\right) + S_L\left(\mathbf{U}_l^* - \mathbf{U}_l\right) & \text{if } S_L \le 0 < S_M \\ \mathbf{F}\left(\mathbf{U}_r\right) + S_R\left(\mathbf{U}_r^* - \mathbf{U}_r\right) & \text{if } S_M \le 0 \le S_R \\ \mathbf{F}\left(\mathbf{U}_r\right) & \text{if } S_R < 0 \end{cases} . \tag{2.5}$$

The wavespeeds S_L and S_R correspond to the left and the right acoustic waves, whereas S_M is related to the intermediate contact/shear characteristic. If the flow is supersonic from left to right, the acoustic wavespeed is $S_L > 0.0$ and the flux has a contribution from the left state only; conversely, the flux is evaluated from the right state in the case of $S_R < 0$. In subsonic conditions the flux evaluation is further subdivided to ensure accuracy at the contact surfaces, where U_l^* and U_r^* are the corresponding states. A detailed description of the scheme can be found in Batten *et al.* (1997).

2.2. *Higher-order reconstruction and slope limiting*

The convective flux evaluation illustrated in the previous section leads to a first-order accurate scheme. Second-order accuracy is typically achieved by computing the states at each side of a given cell face using second-order interpolation and then applying the same flux evaluation scheme to the reconstructed states. On an unstructured grid the reconstruction is formulated as

$$\phi_f^L = \phi_P + \psi_P \left.\nabla\phi\right|_P \cdot \mathbf{r}_f, \tag{2.6}$$

where $\left.\nabla\phi\right|_P$ is a discrete approximation of the gradient at the cell center P, computed using a standard least-squares approximation or the Green-Gauss theorem, ψ_P is the slope-limiter function and r_f is the vector connecting the cell center and the center of the face f. Across a discontinuity and, in general, in regions where the solution changes rapidly, the slope-limiter function ψ_P reduces the discrete gradient such that the reconstructed value at the face center maintains monotonicity. In Berger *et al.* (2005) slope limiters are reviewed as well as issues that can arise on unstructured grids.

We implemented the limiter procedure first proposed by Barth & Jespersen (1989) and later improved by Venkatakrishnan (1995). The limiter can be described as follows:

$$\psi_f = \begin{cases} \psi\left(\frac{\delta_+}{\delta_-}\right), & \text{with } \delta_+ = \phi_{\max} - \phi_P \quad \text{if } \phi_f > \phi_P, \\ \psi\left(\frac{\delta_+}{\delta_-}\right), & \text{with } \delta_+ = \phi_{\min} - \phi_P \quad \text{if } \phi_f < \phi_P, \\ 1 & \qquad\qquad\qquad\qquad\qquad \text{if } \phi_f = \phi_P, \end{cases} \tag{2.7}$$

where $\delta_- = \phi_f - \phi_P$ and $\phi_{\max}$ and $\phi_{\min}$ are the maximum, respectively, and the minimum values of ϕ_P and at all neighboring cell centroids. The limiter function is defined as

$$\psi\left(\frac{\delta_+}{\delta_-}\right) = \frac{\delta_+^2 + 2\delta_+\delta_- + \varepsilon^2}{\delta_+^2 + \delta_+\delta_- + 2\delta_-^2 + \varepsilon^2}. \tag{2.8}$$

The final limiter value ψ_P in Eq. (2.6) is obtained by taking the minimum of all face values ψ_f enclosing the cell centroid P. The parameter ε^2 is introduced to avoid division by zero in regions where ϕ is constant and is taken to be $\varepsilon^2 = (K\Delta x)^3$, with K a user-specified constant and Δx a characteristic length representing the local mesh size (Venkatakrishnan 1995). Revisiting Eq. (2.8) and the definition of ε, one can see that in order to achieve unit consistency, the user-specified constant K bears the units from the mesh size and the limiting variable ϕ, which makes it less favorable as mesh independency is introduced. To achieve unit consistency we propose a different definition of ε, with

$$\varepsilon = K\phi_{ref}, \tag{2.9}$$

where ϕ_{ref} represents a strictly positive field of the same units as ϕ, e.g., for limiting the slope of the velocity across a shock we take ϕ_{ref} to be the speed of sound. The constant K defines the amount of ϕ_{ref} to be taken. A value of zero implies that the limiter is active even in near-constant regions, whereas a very high value for K implies no limiting at all. The limiter is expected to ameliorate convergence, however, depending on the value of K (Pečnik *et al.* 2009).

2.3. *Viscous fluxes*

The viscous fluxes contain second derivatives of the velocity $\mathbf{u}$ and the enthalpy h. Therefore, gradients at the cell face need to be calculated in an efficient and accurate way. Consider the scalar quantity ϕ whose gradient at the cell face is $\nabla\phi$. We approximate the normal gradient at the face as

$$\nabla\phi|_f \cdot \mathbf{n}_f = \frac{\phi_{nbr} - \phi_P}{|\mathbf{x}_{nbr} - \mathbf{x}_P|}\alpha_f + \frac{1}{2}\left(\nabla\phi|_P + \nabla\phi|_{nbr}\right) \cdot \left(\mathbf{n}_f - \alpha_f \mathbf{s}_f\right), \tag{2.10}$$

where the subscript f indicates the face with the adjacent control volumes P and its neighbor nbr (Ham & Iaccarino 2004). The vector $\mathbf{n}$ is the face normal and $\mathbf{s}$ is the normalized vector connecting the cell centroid across the face f. The gradients $\nabla\phi$ at the cell centers are computed using the Green-Gauss theorem and α is chosen to be the dot product $\alpha = \mathbf{s} \cdot \mathbf{n}$.

2.4. *Implicit pseudo-time integration to steady state*

The discretization of the spatial terms in the Navier-Stokes equations results in a large coupled set of ordinary differential equations of the form given in Eq. (2.3). An implicit scheme is obtained by evaluating the spatial residual terms at the new time level $n+1$ (backward Euler). Since these quantities are not known explicitly, a linearization must be performed about the current time level leading to (Mavriplis 1997):

$$\left(\frac{\mathbf{I}}{\Delta t} + \frac{\partial \mathbf{R}}{\partial \mathbf{U}}\right)\Delta\mathbf{U} = -\mathbf{R}\left(\mathbf{U}^n\right). \tag{2.11}$$

A Taylor expansion is used to formulate the Jacobian matrices for the inviscid and viscous fluxes:

$$\mathbf{F}^{n+1} \approx \mathbf{F}^n + \left.\frac{\partial \mathbf{F}}{\partial \mathbf{U}}\right|^n \delta\mathbf{U} + O\left(\delta\mathbf{U}\right)^2 . \tag{2.12}$$

The implicit form of the HLLC scheme is based on the decomposition of the wavespeeds reported in Eq. (2.5):

$$\mathbf{F}^{n+1}_{HLLC} = \begin{cases} \mathbf{F}^n_l + \frac{\partial \mathbf{F}_l}{\partial \mathbf{U}_l}\delta\mathbf{U}_l \\ \mathbf{F}^n_l + S^n_L\left(\mathbf{U}^{*n}_l - \mathbf{U}^n_l\right) + \left[\frac{\partial \mathbf{F}_l}{\partial \mathbf{U}_l} + S^n_L\left(\frac{\partial \mathbf{U}^*_l}{\partial \mathbf{U}_l} - \mathbf{I}\right)\right]\delta\mathbf{U}_l + S^n_L\frac{\partial \mathbf{U}^*_l}{\partial \mathbf{U}_r}\delta\mathbf{U}_r \\ \mathbf{F}^n_r + S^n_R\left(\mathbf{U}^{*n}_r - \mathbf{U}^n_r\right) + \left[\frac{\partial \mathbf{F}^n_r}{\partial \mathbf{U}_r} + S^n_R\left(\frac{\partial \mathbf{U}^*_r}{\partial \mathbf{U}_r} - \mathbf{I}\right)\right]\delta\mathbf{U}_r + S^n_R\frac{\partial \mathbf{U}^*_r}{\partial \mathbf{U}_l}\delta\mathbf{U}_l \\ \mathbf{F}^n_r + \frac{\partial \mathbf{F}_r}{\partial \mathbf{U}_r}\delta\mathbf{U}_r \end{cases}, \tag{2.13}$$

with the Jacobian matrix $\partial\mathbf{F}/\partial\mathbf{U}$ and the matrix $\partial\mathbf{U}^*/\partial\mathbf{U}$, which are given in Batten *et al.* (1997).

The viscous flux is linearized as

$$\mathbf{F}^{n+1}_v = \mathbf{F}^n_v + \frac{\partial \mathbf{F}_v}{\partial \mathbf{U}_l}\delta\mathbf{U}_l + \frac{\partial \mathbf{F}_v}{\partial \mathbf{U}_r}\delta\mathbf{U}_r \tag{2.14}$$

with

$$\frac{\partial \mathbf{F}_v\left(\mathbf{U}\right)}{\partial \mathbf{U}} = \mathbf{A}_v = \frac{\partial \mathbf{F}_v\left(\mathbf{Q}\right)}{\partial \mathbf{Q}}\frac{\partial \mathbf{Q}}{\partial \mathbf{U}} , \tag{2.15}$$

and with $\mathbf{Q} = [0\ u\ v\ w\ T\ \phi_i]^T$ and $\partial\mathbf{Q}/\partial\mathbf{U}$ based on Pulliam & Steger (1982).

The resulting large sparse system (the Jacobian matrices are obtained using first-order discretization) is solved with the generalized minimal residual method (GMRES),

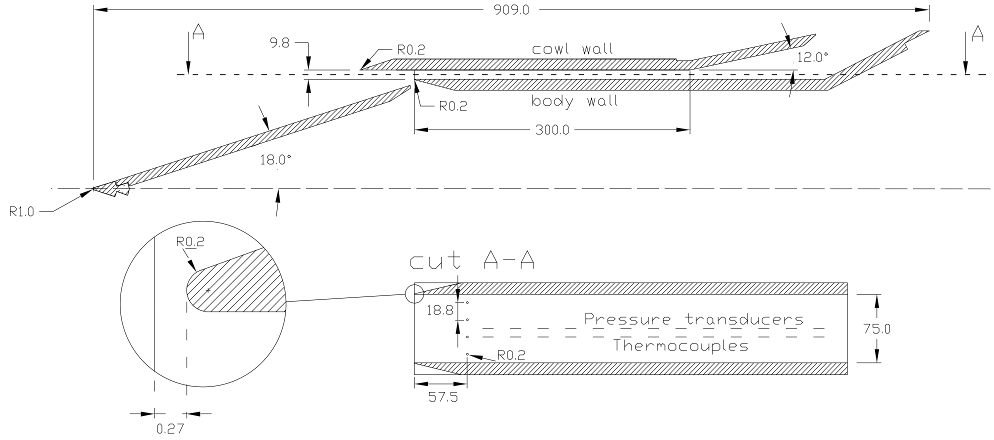

FIGURE 1. Details of the Hyshot II geometry.

preconditioned with the incomplete LU (ILU) factorization, using the freely available linear solver package PETSc (Satish *et al.* 2001).

3. Hyshot II ground experiment: Geometry and test conditions

The ground-based experiment in the High Enthalpy Shock Tunnel (HEG) at the German Aerospace Center (DLR) of a 1:1 model of the HyShot II vehicle (Gardner *et al.* 2004; Karl *et al.* 2008) is investigated in this study. This ground-based experiment provides a more comprehensive data set and better-defined boundary conditions than the original HyShot II scramjet flight experiment. The experiment provides pressure and heat transfer measurements for fuel-off and fuel-on conditions at the wedge intake and the combustor top and bottom wall, as given in Figure 1. The overall Hyshot II scramjet geometry is given in the same figure, where the flow path is from left to right. It consists of a wedge intake and a combustor with constant area terminated by an exhaust nozzle. A bleed channel is located just before the entrance of the combustor to swallow the shock induced by the leading edge of the combustor top wall and the boundary layer on the intake ramp. Cut A-A shows the combustor top view with the four porthole injectors and the blunt combustor side walls.

The free stream flow conditions are given in Hannemann *et al.* (2010) and summarized in Table 1. The total conditions are obtained by averaging over 13 test runs (4 non-reactive and 9 reactive tests) that were performed in the HEG shock tunnel at the DLR, Göttingen, Germany. The static conditions are derived from these averaged total conditions and are also reported in Hannemann *et al.* (2010). In order to estimate the static conditions for the individual runs the ratios of P_s/P_0, T_s/T_0 and $U/\sqrt{H_0}$ are assumed constant and scaled by the individual total conditions at the nozzle exit. The corresponding static conditions for the four non-reactive tests are given in Table 2.

4. Results for the non-reactive cases

The flow field inside the Hyshot II combustor was simulated using five different meshes, summarized in Table 3. In order to investigate the effect of the combustor side walls, a 2D approximation and a full 3D mesh (mesh 1 and 2) including both side walls was

		Total	Static
Pressure	[Pa]	$177.30 \cdot 10^5$	2064.25
Temperature	[K]	2738.23	263.6
Enthalpy	[J/kg]	$3.24 \cdot 10^6$	–
Velocity	[m/s]	2398	
Mach number	[–]	7.355	
Gas constant	[J/kgK]	288.22	
Hydrogen pressure	[Pa]	$5.04 \cdot 10^5$	
Hydrogen temperature	[K]	300	
Equivalence ratio	[–]	3.14	
Angle of attack	[deg]	3.6	
Wall temperature	[K]	300	

Table 1. Averaged boundary conditions for the Hyshot II ground experiment (Hannemann *et al.* 2010).

HEG Exp. no.	p_{st} [Pa]	T_{st} [K]	U [m/s]	P_{ref} [Pa]	Q_{ref} [W/m^2]
805	2072.98	268.2	2401.7	$1.7805 \cdot 10^7$	$1.2448 \cdot 10^{10}$
807	2109.54	271.62	2420.1	$1.8119 \cdot 10^7$	$1.2770 \cdot 10^{10}$
808	2040.62	265.65	2386.87	$1.7527 \cdot 10^7$	$1.2183 \cdot 10^{10}$
814	2056.57	267.51	2398.0	$1.7664 \cdot 10^7$	$1.2356 \cdot 10^{10}$

Table 2. Individual static boundary conditions and reference values for the four non-reactive tests.

Mesh	Geometry	Injector	Side wall	Refinement	Mesh cells
1	2D	no	no	no	0.2M
2	3D full span	no	yes	no	9.0M
3	3D 1/8 span	yes	no	no	2.6M
4	3D 1/8 span	yes	no	yes	14.8M
5	3D 1/2 span	yes	yes	no	12.6M

Table 3. Different meshes used for the validation.

used for fuel-off conditions without the porthole injectors. The mesh sizes for the 2D and for the full 3D meshes are 0.2M and 9.0M, respectively. The influence of adaptive mesh refinement was studied using mesh 3 and 4, while the refined mesh consists of almost six times more mesh cells. Both meshes include the porthole injectors, and fuel mixing without reaction was simulated. The results obtained with mesh 5 are presented in Part 2 of this paper: Reactive cases.

Figure 2 shows the comparison between the 2D simulations using the Menter SST turbulence model (Menter 1994) and the experiments for the four non-reactive cases (Table 2) obtained on mesh 1. Excellent agreement between the numerical and experimental

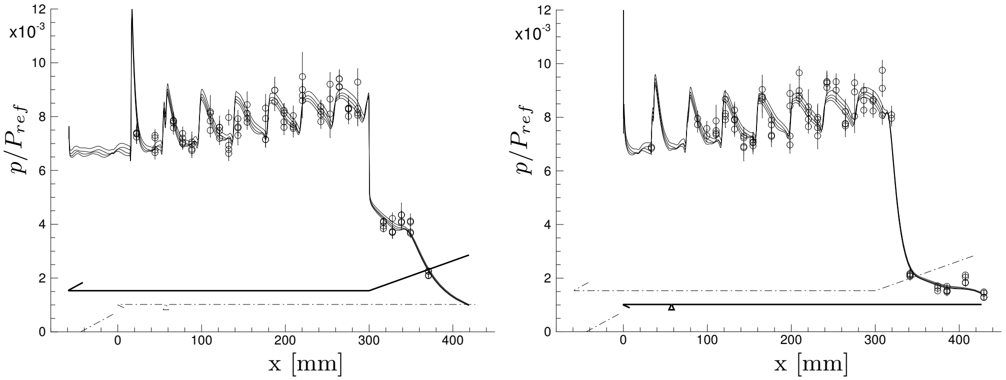

(a) normalized pressure, cowl side (b) normalized pressure, body side

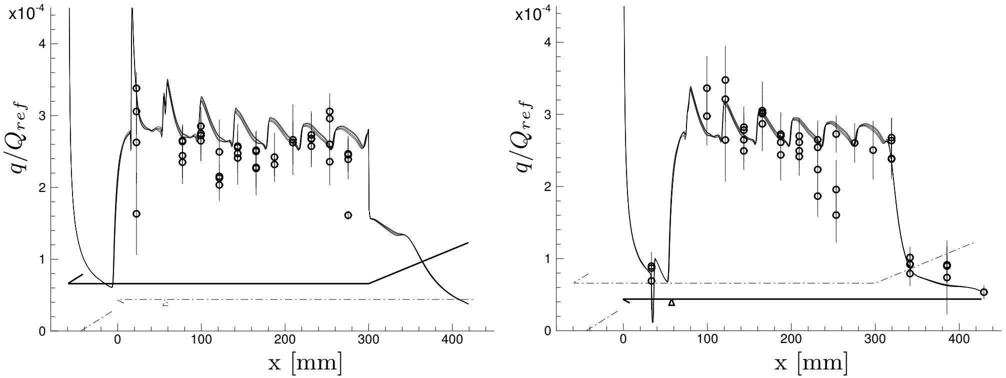

(c) normalized heat flux, cowl side (d) normalized heat flux, body side

FIGURE 2. 2D results using the Menter SST turbulence model (solid lines) for the pressure along the cowl (a) and body walls (b) and the normalized heat flux along the cowl (c) and body walls (d) compared to the four non-reactive (fuel-off) experimental runs (symbols with error bars) for the conditions as given in Table 2.

surface pressure distributions was achieved on both walls, Figure 2(a) and 2(b). All results (experimental and numerical) are normalized with their corresponding reference values, also given in Table 2. The observed pressure oscillations are caused by the shock train inside the combustor (reflections of the body-side blunt leading edge shock shown in Figure 4 (top)). Only a small variability of the pressure distribution is seen for both the numerical and experimental results. Figures 2(c) and 2(d) show the results for the heat flux distribution. Transition from laminar to turbulent flow inside the boundary layers was set according to experimental measurements 50 mm downstream of the leading edges of the respective combustor walls (Karl *et al.* 2008), also indicated by the large increase of the heat flux at these locations. Interestingly, unlike the measurements, the simulations for the four non-reactive simulations do not show a large variability of the heat flux. The strong variability in the experiments indicates the difficulty in obtaining accurate and consistent heat flux measurements in a short-duration test facility under these extreme flow conditions. For the 2D simulations grid convergence was reached with 120 cells in wall normal ($y^+ < 1.0$) and 800 cells in streamwise direction within the combustor (mesh 1 in Table 3).

The influence of different turbulence models and geometrical fidelity on the pressure

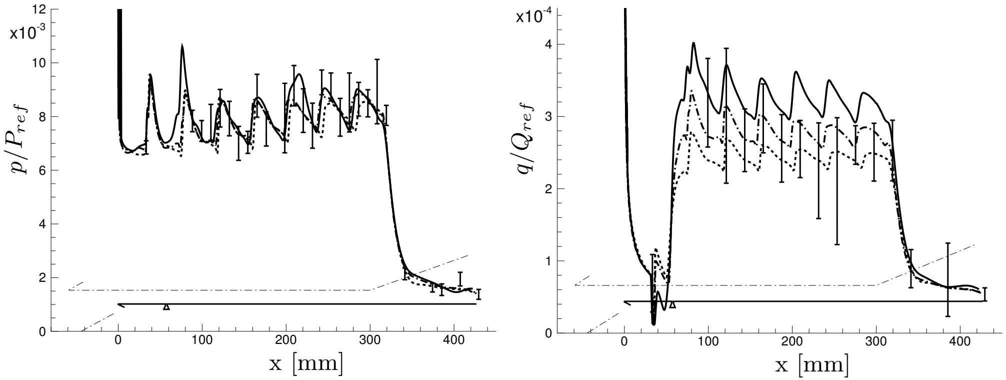

(a) normalized pressure, body side (b) normalized heat flux, body side

FIGURE 3. Results for normalized pressure (a) and heat flux (b) along the body wall with the Spalart and Allmaras (dotted line) and the Menter SST turbulence model (dash-dotted line), both on the 2D mesh, and the full 3D result including side walls with the Menter SST turbulence model (solid line). Reference values are: $P_{ref} = 17.7$MPa and $Q_{ref} = 1.237 \cdot 10^{10}$W/m^2.

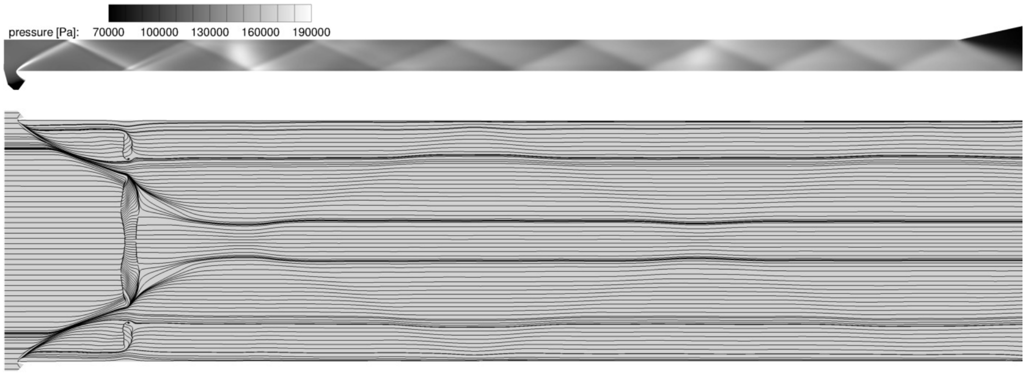

FIGURE 4. Full 3D result: pressure contour plot in the symmetry plane showing the shock train (top) and wall friction lines at the body wall indicating the boundary layer separation at the first shock reflection (bottom).

and heat flux distributions along the body wall is shown in Figure 3, obtained using the averaged conditions given in Table 1. Only the 3D simulation including the side walls shows large differences in the pressure distribution compared to the 2D results with different turbulence models (see Figure 3(a)). The induced shocks at the side walls intersect at two positions at the center plane, which results in an increased pressure compared to the 2D simulations. The influence of the different turbulence models on the surface heat flux in Figure 3(b) is more pronounced than for the pressure. The 2D result with the Spalart and Allmaras turbulence model (Spalart & Allmaras 1994) gives a lower heat transfer in the turbulent boundary layer after the transition than the Menter SST model on the same mesh. Interestingly, the 3D simulation with the side wall and the Menter SST model further increases the simulated heat transfer, leading to a better agreement with the measurements behind the transition but a stronger deviation further downstream in the combustor ($x > 140$ mm). The heat flux increase can be explained by the 3D boundary layer separation induced by the side wall shocks and the shock train, as indicated in Figure 4 (bottom) by means of the wall friction lines at the body wall.

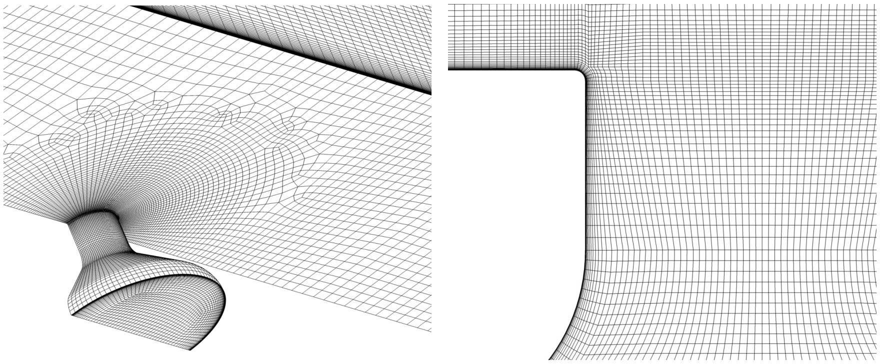

(a) injector and body side mesh (b) modeled radius at body wall and injector

Figure 5. Mesh details for model with the porthole injector.

The 3D computational mesh with the porthole injectors showing the body wall and one symmetry plane in the vicinity of the injector is presented in Figure 5(a). In order to increase numerical stability, a corner radius at the injector of 0.06 mm was used 5(b) (Karl *et al.* 2008). The baseline mesh consists of 2.6 M hexahedral cells that are clustered in wall-normal direction to ensure $y^+ < 1.0$.

In order to verify mesh convergence, a successive two-level adaptive mesh refinement (AMR) based on the negative velocity divergence $\nabla \cdot u$ was applied. The refinement indicator for the first and second levels were set to $L_1 = -1 \cdot 10^5$ and $L_2 = -2 \cdot 10^5$, respectively. The baseline and the AMR mesh are compared in a plane parallel to the body wall located at y/d = 2 in Figure 6(a). Figure 6(b) shows the pressure contour obtained on the baseline and the AMR mesh. The solution obtained on the refined mesh shows sharper shock structures, although the flow structures appear to be the same on both meshes. The obtained pressure and heat flux distributions are compared in Figure 7. Minor differences are observed only for the heat flux (Figure 7(b)), with more pronounced peaks for the AMR result.

Figure 8 illustrates the complex flow field of the non-reactive fuel-mixing simulation within the Hyshot II combustor using the result obtained with the AMR mesh. The contour plots show the pressure in the combustor symmetry plane and a plane parallel to the body wall at $y/d \sim 4$. The penetrations of the hydrogen jets induce strong bow- and separation-shocks in front of the porthole injectors. These shocks intersect with the shock train and create a complex multiple shock system further downstream in the combustor. The low pressure regions (dark color) behind the porthole injectors indicate the jet wake.

5. Conclusion and future work

A fully implicit parallel Reynolds-averaged Navier-Stokes code based on a finite volume formulation on arbitrary polyhedral mesh elements was developed and applied to simulate the flow field inside the Hyshot II combustor. Different geometrical fidelity levels and different turbulence models were used for the validation study. Simulations of the full combustor (including the side walls) showed the highest heat flux at the body wall after transition compared to the 2D simulations, due to a highly three-dimensional separation induced by the shock train and the side wall shocks. The results for the pressure

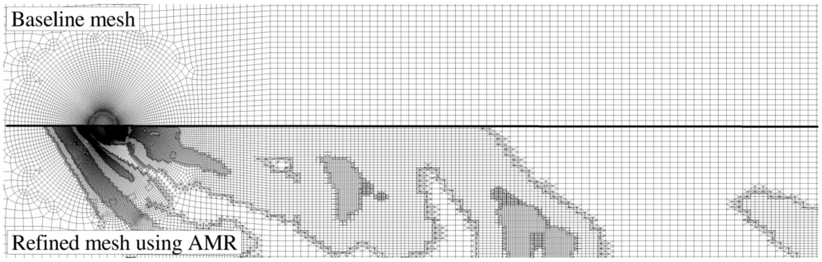

(a) Mesh parallel to the bottom wall of the combustor located at y/d = 2. Top: baseline, bottom: AMR refined

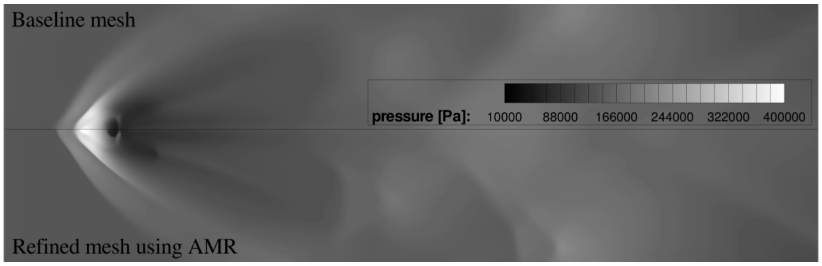

(b) Pressure contour parallel to the bottom wall of the combustor located at y/d = 2, top: baseline, bottom: AMR refined

FIGURE 6. Mesh and pressure comparison between baseline and AMR mesh at a plane above the body wall.

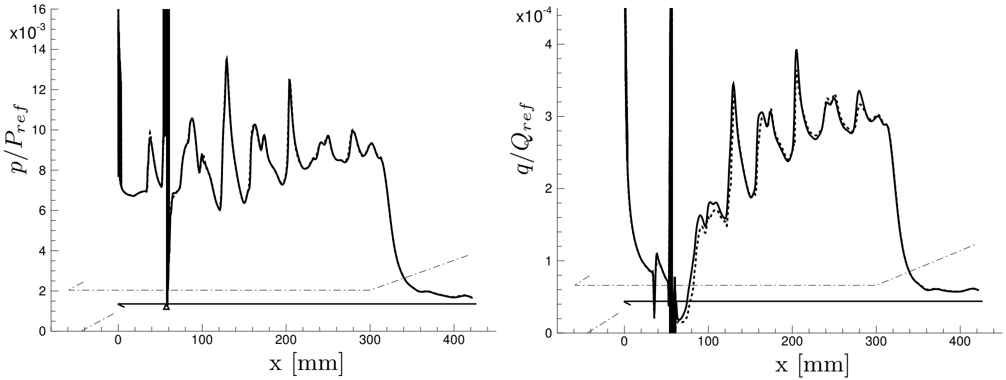

(a) normalized pressure: body side

(b) normalized flux flux: body side

FIGURE 7. Results for normalized pressure (a) and heat flux (b) along the body wall. AMR: solid line, baseline mesh: dashed line. No measurements are available for pure fuel mixing.

distributions are in excellent agreement with the experiments, whereas no clear conclusion can be made for the heat flux due to the large variability of the measurement data from the experiments. Furthermore, a mesh convergence study was performed for the 1/8 span combustor simulation including the hydrogen injectors using adaptive mesh refinement along the shocks present in the combustor. The simulations showed that grid convergence was achieved using the baseline mesh, which is subsequently used for the reactive simulations discussed in Part 2.

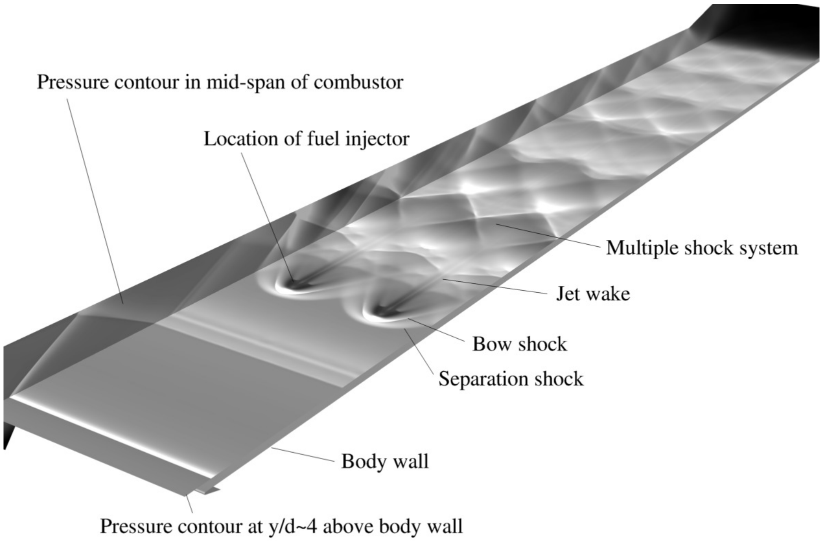

FIGURE 8. Pressure contours illustrating the complexity of the flow.

Acknowledgments

The authors would like to thank Dr. K. Hannemann and S. Karl (German Aerospace Center, DLR, Germany) for providing the experimental data and for their help. This work was supported by the US Department of Energy under the Predictive Science Academic Alliance Program (PSAAP) Program.

REFERENCES

BARTH T.J., JESPERSEN, D.C. 1989 The design and application of upwind schemes on unstructured meshes. 27th Aerospace Science Meeting, Reno, NV, AIAA 1989-0366

BATTEN, P. LESCHZINER, M. A., & GOLDBERG, U. C. 1997 Average-state Jacobeans and implicit methods for compressible viscous and turbulent flows. *J. Comput. Physics* **137**, 38-78.

BERGER, M., AFTOSMIS, M. J. & MURMAN, S. M. 2005 Analysis of slope limiters on irregular grids. 43rd Aerospace Science Meeting, Reno, NV, AIAA 2005-0490.

CANDLER, G. V., BARNHARDT, M. D., DRAYNA, T. W., NOMPELIS, I., PETERSON, D. M. & S SUBBAREDDY, P. 2007 Unstructured grid approaches for accurate aeroheating simulations. 18th AIAA Computational Fluid Dynamics Conference, Miami, US., AIAA 2007-3959.

DRUGUET, M. C., CANDLER, G. V. & NOMPELIS, I. 2005 Effect of numerics on Navier-Stokes computations of hypersonic double-cone flows. *AIAA Journal.* **43-3**, 616-623.

EINFELDT, B., MUNZ, C. D, ROE, P. L. & SJOGREEN, B. 1991 On Godunov-type methods near low densities. *J. Comput. Physics* **92**, 273.

GARDNER, A. D., HANNEMANN, K., STEELANT, J. & PAULL, A. 2004 Ground testing of the HyShot supersonic combustion flight experiment in HEG and comparison with flight data. *AIAA Paper 2004-3345.*

HAM, F. & IACCARINO, G. 2004 Energy conservation in collocated discretization schemes on unstructured meshes. *Annual Research Briefs. Stanford, Calif.: Center for Turbulence Research, Stanford*, pp 3-14.

Hannemann, K., Karl, S., Schramm, J.M. & Steelant, J. 2010 Methodology of a combined ground based testing and numerical modelling analysis of supersonic combustion flow paths. *Shock Waves* **20**, 353366

Karl, S., Hannemann, K., Mack, A. & Steelant, J. 2008 CFD analysis of the HyShot II scramjet experiments in the HEG shock tunnel. 15th AIAA International Space Planes and Hypersonic Systems and Technologies Conference, Dayton, Ohio, AIAA 2008-2548.

Mavriplis, D.J. 1997 Unstructured grid techniques. *Annu. Rev. Fluid Mech.* **29**, 473-514

Menter, F. R. 1994 Two-equation eddy-viscosity turbulence models for engineering applications. *AIAA Journal* **32(8)**, 1598-1605.

Nishikawa, H. & Kitamura, K. 2008 Very simple, carbuncle-free, boundary-layer-resolving, rotated-hybrid Riemann solvers. *J. Comput. Physics* **227**, 2560-2581.

Nompelis, I., Drayna, T. W. & Candler, G. V. 2005 A parallel unstructured implicit solver for hypersonic reacting flow simulation. 17th AIAA Computational Fluid Dynamics Conference, Toronto, Canada., AIAA 2005-4867.

Pečnik, R. , Terrapon, V.E., Ham, F. & Iaccarino, G. 2009 Full system scramjet simulation. Annual Research Briefs, Center for Turbulence Research, Stanford, pp. 33–45.

Pulliam, T. H. & Steger, J. L. 1985 Recent improvements in efficiency, accuracy, and convergence for implicit approximate factorization algorithms. 23rd AIAA Aerospace Sciences Meeting. Reno, Nev. 38, AIAA-1985-360.

Quirk, J. J. 1994 A contribution to the great Riemann solver debate. *Int. J. Numer. Methods Fluids* **18**, 555.

Roe, P. L., 1981 Approximate Riemann solvers, parameter vectors, and difference schemes. *J. Comput. Phys.* **43**, 357-372.

Sanders, R., Morano, E. & Druguet, M. C. 1998 Multidimensional dissipation for upwind schemes: stability and applications to gas dynamics. *J. Comput. Physics,* **145**, 511-537.

Satish, B., Buschelman, K., Eijkhout, V., Gropp, W.D., Kaushik, D., Knepley, M.G., McInnes, L.C., Smith, B.F., & Zhang, H. 2009 PETSc Web page, http://www.mcs.anl.gov/petsc.

Smart, M. K., Hass, N. E. & Paull, A. 2006 Flight data analysis of the HyShot 2 scramjet flight experiment. *AIAA Journal* **44**(10), 2366–2375.

Spalart, P. R. & Allmaras, S. R. 1994 A one-equation turbulence model for aerodynamic flows. *Recherche Aerospatiale* **1**, 5-21.

Toro, E. F. 1999 Riemann Solvers And Numerical Methods For Fluid Dynamics. A Practical Introduction. New York, Springer.

Toro, E. F., Spruce, M. & Spears, W. 1994 Restoration of the contact surface in the HLL-Riemann solver *Shock Waves* **4**, 25-34.

Van Leer, B., Lee, W. T. & Powell, K. G. 1989 Sonic-point capturing. 9th Computational Fluid Dynamics Conference. Buffalo, NY., *AIAA Paper* 89-1945-CP

Venkatakrishnan, V. 1995 Convergence to steady state solutions of the Euler equations on unstructures grids with limiters. *J. Comput. Phys.* **118**, 120-130